

See discussions, stats, and author profiles for this publication at: <https://www.researchgate.net/publication/271273634>

# Understanding Solvothermal Crystallization of Mesoporous Anatase Beads by In Situ Synchrotron PXRD and SAXS

ARTICLE in CHEMISTRY OF MATERIALS · AUGUST 2014

Impact Factor: 8.35 · DOI: 10.1021/cm501810x

---

CITATIONS

4

READS

106

## 9 AUTHORS, INCLUDING:



Dehong Chen

University of Melbourne

52 PUBLICATIONS 2,277 CITATIONS

[SEE PROFILE](#)



Deborah Lau

The Commonwealth Scientific and Industrial ...

61 PUBLICATIONS 703 CITATIONS

[SEE PROFILE](#)



Matteo Leoni

Università degli Studi di Trento

238 PUBLICATIONS 2,548 CITATIONS

[SEE PROFILE](#)



J. Ilavsky

Argonne National Laboratory

222 PUBLICATIONS 3,181 CITATIONS

[SEE PROFILE](#)

# Understanding Solvothermal Crystallization of Mesoporous Anatase Beads by In Situ Synchrotron PXRD and SAXS

Fang Xia,<sup>†,‡</sup> Dehong Chen,<sup>§</sup> Nicola V. Y. Scarlett,<sup>‡</sup> Ian C. Madsen,<sup>‡</sup> Deborah Lau,<sup>†</sup> Matteo Leoni,<sup>||</sup> Jan Ilavsky,<sup>†</sup> Helen E. A. Brand,<sup>‡,#</sup> and Rachel A. Caruso\*,<sup>†,‡,§</sup>

<sup>†</sup>CSIRO Materials Science and Engineering, Clayton, VIC 3168, Australia

<sup>‡</sup>CSIRO Process Science and Engineering, Clayton, VIC 3168, Australia

<sup>§</sup>Particulate Fluids Processing Centre, School of Chemistry, The University of Melbourne, Melbourne, VIC 3010, Australia

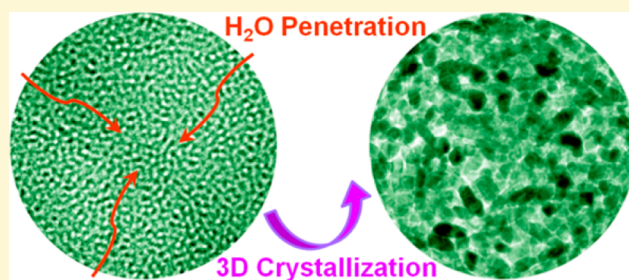
<sup>||</sup>Department of Civil, Environmental and Mechanical Engineering, University of Trento, 38123 via Mesiano 77, Trento, Italy

<sup>†</sup>Advanced Photon Source, Argonne National Laboratory, 9700 South Cass Avenue, Argonne, Illinois 60439, United States

<sup>#</sup>Australian Synchrotron, 800 Blackburn Rd., Clayton, VIC 3168, Australia

## S Supporting Information

**ABSTRACT:** Submicrometer-sized mesoporous anatase ( $TiO_2$ ) beads have shown high efficiency as electrodes for dye-sensitized solar cells and are recoverable photocatalysts for the degradation of organic pollutants. The detailed mechanism for crystallization of the amorphous  $TiO_2$ /hexadecylamine (HDA) hybrid beads occurring during the solvothermal process needs to be understood so that reaction parameters can be rationally refined for optimizing the synthesis. In this work, the solvothermal crystallization was monitored by in situ synchrotron powder X-ray diffraction (PXRD) and synchrotron small-angle X-ray scattering (SAXS) techniques. In situ PXRD provided crystallization curves, as well as the time evolution of anatase crystallite mean size and size distribution, and in situ SAXS provided complementary information regarding the evolution of the internal bead structure and the formation of pores during the course of the solvothermal process. By exploring the effects of temperature (140–180 °C), bead diameter (300 and 1150 nm), bead internal structure, and solvent composition (ethanol and ammonia concentrations) on this process, the crystallization was observed to progress 3-dimensionally throughout the entire bead due to solvent entrance after an initial fast partial dissolution of HDA from the nonporous precursor bead. On the basis of the kinetic and size evolution results, a 4-step crystallization process was proposed: (1) an induction period for precursor partial dissolution and anatase nucleation; (2) continued precursor dissolution accompanied by anatase nucleation and crystal growth; (3) continued precursor dissolution accompanied by only anatase crystal growth; and (4) complete crystallization with no significant Ostwald ripening.



## 1. INTRODUCTION

Titanium dioxide ( $TiO_2$ ) is an important metal oxide due to its wide application in areas such as paint (as a white pigment), photocatalysis, energy storage and conversion, and sensing.<sup>1</sup> Among many physical and chemical synthesis methods, hydrothermal and solvothermal routes are very versatile for fabricating diverse  $TiO_2$  nanomaterials. For example,  $TiO_2$  with a high percentage of the highly reactive {001} facets was synthesized hydrothermally for enhanced catalysis efficiency;<sup>2,3</sup> hierarchical anatase  $TiO_2$  spheres consisting of nanorods and nanoparticles were prepared solvothermally for dye-sensitized solar cells;<sup>4</sup> and Au-doped  $TiO_2$  nanocomposites were prepared solvothermally for enhanced photocatalytic activity in water treatment applications.<sup>5,6</sup> The crystallite size, size distribution, morphology, crystal structure, and crystallinity of titanium dioxide heavily influence the materials performance in the chosen application. Fundamentally, these characteristics are determined by the crystallization process occurring during

synthesis. Hence, a detailed understanding of this mechanism will benefit the rational design of synthesis for the preparation of materials that are optimized for the area of application. In the literature, the majority of studies focus on materials syntheses or demonstrate potential application, few studies are devoted to understanding the  $TiO_2$  crystallization mechanism under solvothermal or hydrothermal conditions.<sup>7–10</sup>

In situ powder X-ray diffraction (PXRD) and in situ small-angle X-ray scattering (SAXS) are powerful tools for studying hydrothermal/solvothermal synthesis mechanisms. This is because they monitor the synthesis by collecting time-resolved patterns containing direct reaction information, such as phase evolution and the fate of the transient reaction intermediates. Understanding the reaction intermediates can be critical in

Received: May 20, 2014

Revised: June 23, 2014

Published: July 17, 2014

**Table 1.** Summary of in Situ PXRD Experiments and Kinetic Results

run	precursor	solvent	T (°C)	$t_0$ (min) <sup>d</sup>	$t - t_0$ (min) <sup>e</sup>	$k$ (s <sup>-1</sup> ) <sup>f</sup>	$n^g$
PD01	PB(HDA)1150 <sup>a</sup>	67 vol % ethanol	140	24.6	139.4	$2.49 \times 10^{-4}$ ( $\alpha < 0.72$ ) $2.28 \times 10^{-4}$ ( $\alpha > 0.72$ )	1.43 ( $\alpha < 0.72$ ) 2.05 ( $\alpha > 0.72$ )
PD02	PB(HDA)1150	67 vol % ethanol	160	11.4	106.8	$5.00 \times 10^{-4}$ ( $\alpha < 0.8$ ) $3.99 \times 10^{-4}$ ( $\alpha > 0.8$ )	1.04 ( $\alpha < 0.8$ ) 1.64 ( $\alpha > 0.8$ )
PD03	PB(HDA)1150	67 vol % ethanol	180	3.7	46.3	$1.36 \times 10^{-3}$ ( $\alpha < 0.8$ ) $8.23 \times 10^{-4}$ ( $\alpha < 0.8$ )	1.05 ( $\alpha < 0.8$ ) 1.67 ( $\alpha < 0.8$ )
PD04	PB(HDA)300 <sup>b</sup>	67 vol % ethanol	160	12.4	104.6	$4.38 \times 10^{-4}$ ( $\alpha < 0.71$ ) $3.59 \times 10^{-4}$ ( $\alpha > 0.71$ )	1.67 ( $\alpha < 0.71$ ) 1.81 ( $\alpha > 0.71$ )
PD05	PB(HDA free)830 <sup>c</sup>	67 vol % ethanol	140	9.2	18.6	$2.47 \times 10^{-3}$	1.37
PD06	PB(HDA)1150	80 vol % ethanol	160	13.9	203.9	$4.39 \times 10^{-4}$ ( $\alpha < 0.82$ ) $4.66 \times 10^{-4}$ ( $\alpha > 0.82$ )	1.15 ( $\alpha < 0.82$ ) 0.77 ( $\alpha > 0.82$ )
PD07	PB(HDA)1150	91 vol % ethanol	160	16.7	184.5	$3.70 \times 10^{-4}$ ( $\alpha < 0.72$ ) $3.72 \times 10^{-4}$ ( $\alpha > 0.72$ )	1.40 ( $\alpha < 0.72$ ) 0.96 ( $\alpha > 0.72$ )
PD08	PB(HDA)1150	0.45 M ammonia in 67 vol % ethanol	160	12.8	55.2	$6.77 \times 10^{-4}$ ( $\alpha < 0.83$ ) $5.07 \times 10^{-4}$ ( $\alpha > 0.83$ )	1.11 ( $\alpha < 0.83$ ) 2.82 ( $\alpha > 0.83$ )
PD09	PB(HDA)1150	2.16 M ammonia in 67 vol % ethanol	160	40.6	35.4	$9.65 \times 10^{-4}$	2.09

<sup>a</sup>PB(HDA)1150: Amorphous bicontinuous TiO<sub>2</sub>/HDA hybrid beads of 1150 nm in diameter. <sup>b</sup>PB(HDA)300: Amorphous bicontinuous TiO<sub>2</sub>/HDA hybrid beads of 300 nm in diameter. <sup>c</sup>PB(HDA free)830: Amorphous porous HDA-free TiO<sub>2</sub> beads of 830 nm in diameter. <sup>d</sup> $t_0$ : induction time. <sup>e</sup> $t - t_0$ : crystallization time. <sup>f</sup> $k$ : rate constant. <sup>g</sup> $n$ : Avrami exponent.

determining reaction mechanisms, but the intermediates can be missed by ex situ techniques. In situ PXRD/SAXS can also provide synthesis kinetics very efficiently and accurately, which is of vital importance to the scale up of synthesis for eventual commercial scale applications. In recent years, in situ PXRD or SAXS has been successfully applied to understanding the hydrothermal/solvothermal syntheses of a number of materials, mostly metal oxides,<sup>11–13</sup> hydroxides,<sup>14,15</sup> zeolites,<sup>16–18</sup> and sulfate.<sup>19–21</sup>

There have been few in situ PXRD/SAXS studies for understanding the hydrothermal or solvothermal crystallization of TiO<sub>2</sub>. Hummer and co-workers investigated the formation of TiO<sub>2</sub> nanocrystals from aqueous TiCl<sub>4</sub> solutions at 100 and 200 °C and observed crystallization of both anatase and rutile at the early stage of synthesis, but with prolonged time, rutile continued to grow at the expense of anatase.<sup>7</sup> Iversen and co-workers studied the formation of TiO<sub>2</sub> nanocrystals under supercritical or subsupercritical conditions<sup>8,9</sup> and found that the crystallite size of anatase nanocrystals was influenced by temperature, time, and solvent composition. These studies provided insights for simple scenarios where nanocrystals directly crystallize from homogeneous solutions. However, many applications require much more complex TiO<sub>2</sub> architectures that are often synthesized by reacting the pre-prepared amorphous solid precursor with a desired solvent. One such example is monodisperse mesoporous TiO<sub>2</sub> beads of submicrometer size, which were developed as electrode materials for high performance dye-sensitized solar cells,<sup>22,23</sup> and have been tested for enhanced photodegradation of aqueous organic pollutants.<sup>24</sup>

The synthesis of mesoporous TiO<sub>2</sub> beads is a 3-step process:<sup>22,23</sup> (1) the preparation of amorphous TiO<sub>2</sub>/HDA hybrid precursor beads at room temperature, (2) the solvothermal crystallization of such precursor beads at an elevated temperature, and (3) calcination to enhance crystallinity and to remove any organic residues. While the formation of amorphous TiO<sub>2</sub> precursor beads and the effect of calcination have been elucidated,<sup>23</sup> the complex solvothermal crystallization process is yet to be understood. Hence this work was undertaken to gain an understanding of the solvothermal

crystallization mechanism and kinetics in the formation of the mesoporous anatase beads by combined synchrotron in situ PXRD and in situ SAXS techniques. The complicated synthesis mechanism has been elucidated based on the information from in situ PXRD and SAXS resulting in a proposed 3-dimensional dissolution–nucleation–growth mechanism.

## 2. METHODOLOGY

**2.1. Chemicals.** Titanium(IV) isopropoxide (TIP; 97%, Sigma-Aldrich), hexadecylamine (HDA, 90%, Sigma-Aldrich), absolute ethanol (>99.7%, Merck), potassium chloride (AR, BDH), ammonia solution (25%, Merck), and Milli-Q water (18.2 MΩ cm) were used in this study.

**2.2. Precursor Beads Preparation.** Three kinds of amorphous precursor beads were prepared via a sol–gel self-assembly process.<sup>22,23</sup> (1) Amorphous TiO<sub>2</sub>/HDA hybrid beads of 1150 nm in diameter: 7.95 g of HDA was dissolved in 800 mL of ethanol, followed by the addition of 3.20 mL of aqueous KCl (0.1 M) solution. To this solution was added 18.10 mL of TIP under vigorous stirring at ambient temperature. (2) Amorphous TiO<sub>2</sub>/HDA hybrid beads of 300 nm in diameter: 7.95 g of HDA was dissolved in 800 mL of ethanol, followed by the addition of 3.20 mL of aqueous KCl (0.1 M) solution and 5.33 mL of Milli-Q water. To this solution was added 18.10 mL of TIP under vigorous stirring at ambient temperature. (3) Porous amorphous HDA-free TiO<sub>2</sub> beads of 830 nm in diameter: 3.20 mL of water was added to 800 mL of ethanol. To this solution was added 18.10 mL of TIP under vigorous stirring at ambient temperature. All the above preparations formed a milky white suspension that was kept static for 18 h and then centrifuged, and the beads were washed with ethanol three times and dried in air at room temperature.

**2.3. In Situ PXRD.** In situ PXRD experiments were conducted at the Australian Synchrotron Powder Diffraction Beamline. The X-ray energy was 16 keV, and the wavelength (0.7743 Å) was calibrated using a LaB<sub>6</sub> standard (NIST SRM 660b). The starting slurry (mixture of precursor beads and solvent, Table 1) was injected into a quartz glass capillary (1 mm in diameter, 0.05 mm in wall thickness, and 40 mm in length), which was then sealed into a custom-made stainless steel holder initially designed by Norby.<sup>25</sup> External N<sub>2</sub> pressure (2–3 MPa) was applied to the capillary during the synthesis to prevent vaporization of the solvent. The slurry-containing capillary was fixed at beam center and heated (30 °C min<sup>-1</sup>) to synthesis temperatures (140–180 °C) by a hot air blower beneath the capillary. The temperature was monitored by a K-type thermocouple 3.5 mm beneath the capillary, and the temperature was calibrated using a

$\text{KNO}_3$  temperature standard, which has a phase transition temperature at 128 °C and melting temperature at 333.6 °C. In situ diffraction patterns were collected simultaneously using a position sensitive MYTHEN detector<sup>26</sup> over the 2-theta range 1.5–81.5° and with a time resolution of 1.2–8.2 min (depending on the rate of synthesis). Diffraction patterns were analyzed by (1) sequential Rietveld analysis using the TOPAS v4.2 software package (Bruker-AXS) to obtain the crystallization curves and (2) Whole Powder Pattern Modeling (WPPM)<sup>27</sup> using the software PM2K<sup>28</sup> to extract crystallite mean size and size distributions. A detailed description of the data analysis is provided in the Supporting Information.

**2.4. In Situ SAXS.** In situ SAXS experiments were conducted at the Australian Synchrotron SAXS/WAXS Beamline. The X-ray energy was 12 keV, and the wavelength was calibrated using a silver behenate (AgBe) standard. The slurry sample and experimental setup were identical to those used in the in situ PXRD experiments. SAXS patterns were recorded every 1–4 min with 1 s data collection time, in the  $q$  range from 0.0098 to 0.67 Å<sup>-1</sup>. SAXS data was reduced using scatterBrain v1.730 (Australian Synchrotron) and analyzed by the Irena software package.<sup>29</sup> The detailed analysis strategy and procedure are provided in the Supporting Information.

**2.5. SEM and TEM.** The morphologies of the samples were observed by using a field emission environmental scanning electron microscope (Quanta 200F FEI) without metal sputter coating pretreatment. TEM images and selected area electron diffraction (SAED) patterns of the resulting anatase beads were obtained on an FEI Tecnai F20 transmission electron microscope operating at 200 kV. To investigate the interior structures of the beads, the samples were embedded in an LR-white resin and ultramicrotomed using a diamond knife to obtain 60 nm thick sections.

### 3. RESULTS AND DISCUSSION

Amorphous titanium dioxide precursor beads were prepared in the presence and absence of HDA. The beads were monodisperse in size and, depending on synthesis conditions, had a mean diameter of 300, 830, or 1150 nm. The precursor beads prepared in the presence of HDA are nonporous with a specific surface area of 3.3 m<sup>2</sup> g<sup>-1</sup>. They have a wormhole-like internal mesostructure consisting of amorphous TiO<sub>2</sub> domains and HDA (structure directing agent).<sup>23</sup> The precursor beads prepared in the absence of HDA are mesoporous having a specific surface area of 367 m<sup>2</sup> g<sup>-1</sup>. More detailed information regarding the precursor beads has been given as Figure S4 and Table S1 in the Supporting Information.

**3.1. In Situ PXRD.** In total, nine in situ PXRD experiments were carried out under various mild solvothermal synthesis conditions (Table 1), varying in temperature (140–180 °C), precursor bead diameter (1150 and 300 nm), precursor bead structure (with and without HDA), and solvent composition (ethanol and ammonia concentrations). The in situ PXRD patterns show that these syntheses share a similar phase evolution trend in that the amorphous precursor was directly converted to crystalline anatase with no other intermediate phases detected (Figures 1 and S4–S11, Supporting Information). At the beginning of the synthesis, the broad, amorphous peak at around 10.5° 2θ loses intensity with time, suggesting the dissolution of the amorphous precursor beads. This stage is an induction period for nucleation since no crystalline peaks are apparent. Once crystallization commences, the intensity of the anatase peaks rises gradually until crystallization ceases, which is indicated by no further increase in peak intensity.

**3.2. Crystallization Curves.** Rietveld analysis of PXRD patterns provided quantitative information regarding the extent of crystallization with time. Here the extent of crystallization was calculated by dividing the refined scale factor of the

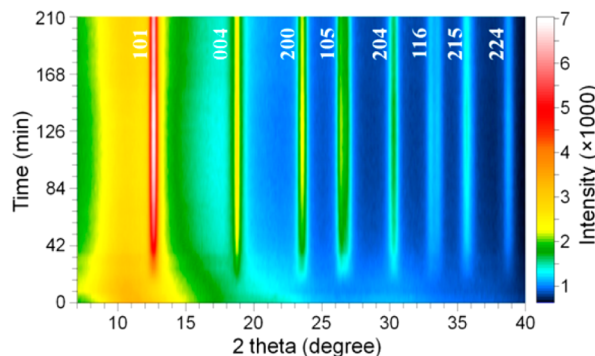


**Figure 1.** Time evolution of in situ PXRD patterns (viewed down the intensity axis) for PD02 crystallization of bicontinuous TiO<sub>2</sub>/HDA hybrid beads of 1150 nm diameter in 67 vol % ethanol at 160 °C. All the diffraction peaks are indexed to anatase. In situ PXRD for the other runs are provided in the Supporting Information (Figures S5–S12).

individual PXRD patterns by the refined scale factor from a pattern where crystallization was considered to be complete. The nucleation and crystallization behavior was influenced by various synthesis conditions.

Temperature plays a significant role in crystallization (Figure 2a). For the synthesis using 1150 nm HDA-containing

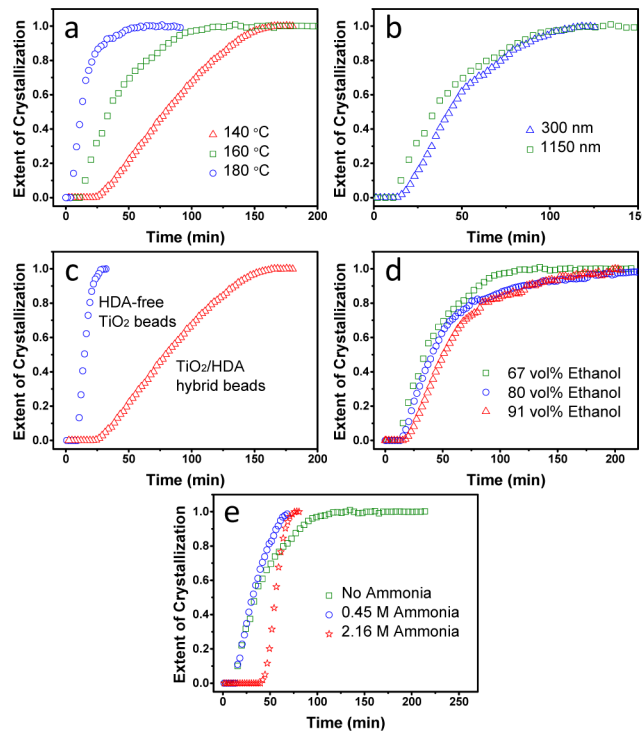


**Figure 2.** Crystallization curves comparing the effect of (a) temperature (PD01, PD02, and PD03), (b) precursor bead size (PD02 and PD04), (c) precursor bead composition (PD01 and PD05), (d) ethanol concentration (PD02, PD06, and PD07), and (e) ammonia concentration (PD02, PD08, and PD09).

precursor beads and 67 vol % ethanol, the synthesis at 140 °C (PD01) took 165 min to complete including an induction period of 24.6 min; after the induction period, slow crystallization occurred and continued to completion. At higher temperatures, however, both crystallization time and induction time were shortened; at 160 °C (PD02), the synthesis took

115 min to complete with 11.4 min induction time; and the synthesis at 180 °C (PD03) was the most rapid, with a 3.7 min induction period, and the completion of crystallization occurred within 50 min.

The size of the precursor beads appears to have little influence on crystallization rate (Figure 2b). In a comparison between crystallization curves at 160 °C using 1150 nm (PD02) and 300 nm (PD04) precursor beads, we see that both syntheses reached complete crystallization at a similar time (~115 min), and they also share a similar induction time (~12 min). This behavior suggests a size-independent crystallization rate. There appears, however, to be a slight difference in the early stage crystallization rate with the larger precursor beads being slightly faster.

The composition of the precursor beads exerts the most profound effect on the crystallization rate (Figure 2c). A comparison between crystallization curves at 140 °C using TiO<sub>2</sub>/HDA hybrid beads (PD01) and HDA-free TiO<sub>2</sub> beads (PD05) shows that both the crystallization and induction period using HDA-free beads was significantly faster than that using TiO<sub>2</sub>/HDA hybrid beads. The synthesis using TiO<sub>2</sub>/HDA hybrid beads took 165 min for complete crystallization with 24.6 min induction time, while the synthesis using HDA-free beads took only 28 min (5 times faster) for complete crystallization with 9.2 min (1.7 times faster) induction time.

Solvent composition variation may also change crystallization behavior (Figure 2d). The initial rate of reaction appeared to slow down with increasing concentration of ethanol, and the induction time looks to have slightly increased with increasing ethanol concentration. The variation after about 75 min is not so clear, and the reaction in 91 vol % ethanol may not have actually reached completion in the available time.

The addition of ammonia to the 67 vol % ethanol significantly altered the crystallization behavior (Figure 2e). Both the induction times and the crystallization curve for the synthesis with 0.45 M ammonia (PD08) almost overlap with the synthesis without ammonia (PD02) when the extent of crystallization was below 0.4; however, after that, the synthesis with 0.45 M ammonia sped up rapidly. The synthesis with 2.16 M (PD09) ammonia showed the most distinctly different behavior, having a very long induction time (41 min) followed by a very rapid crystallization period (35 min). This is probably due to the fact that a high concentration of ammonia increases the solution pH, hence leading to a relatively high solubility of the Ti species. That is, the supersaturation concentration is higher for nucleation to occur, therefore leading to a longer induction time. This result is in good agreement with an early study that explored the effect of ammonia concentration to the morphology of mesoporous TiO<sub>2</sub> beads.<sup>30</sup> The authors suggested the formation of an ammonium titanate metastable phase before the nucleation of anatase. The metastable phase was not observed in this in situ PXRD study, probably due to the relatively low quantity and poor crystallinity of this metastable phase.

**3.3. Synthesis Mechanism: 3-Dimensional Crystallization.** After the solvothermal synthesis, the product beads appear to have preserved the spherical shape of the precursor beads. Normally, shape preservation in solvent-assisted crystallization follows a 2-dimensional (2D) phase boundary controlled crystallization mechanism.<sup>31–36</sup> This mechanism means that the dissolution and crystallization starts from the outer surface of the solid precursor and gradually progresses toward the interior of the precursor. This mechanism is,

however, not supported by our in situ PXRD findings. The reaction rate for 2D crystallization should be proportional to the specific surface area (inversely proportional to the precursor size) as the crystallization progresses only at the precursor–product interface,<sup>32</sup> but our kinetic results indicate a size insensitive crystallization rate. The synthesis using small (300 nm) precursor beads was similar to the synthesis using large (1150 nm) precursor beads under identical conditions (Figure 2c), rather than ~4 times faster as expected from the 2D crystallization mechanism.

The size-independent synthesis rate suggests a 3-dimensional (3D) crystallization process. To confirm this, selected area electron diffraction (SAED) was conducted on an ultramicrotomed cross section of a bead at a crystallization extent of about 0.75, and indeed, similar anatase diffraction patterns in the core and at the edge of the bead were observed (Figure 3), confirming the 3D crystallization mechanism. If the crystallization progresses from the surface to the core via a typical 2D mechanism, the area in the core region (as indicated within the dashed circle in Figure 3) would be the amorphous precursor

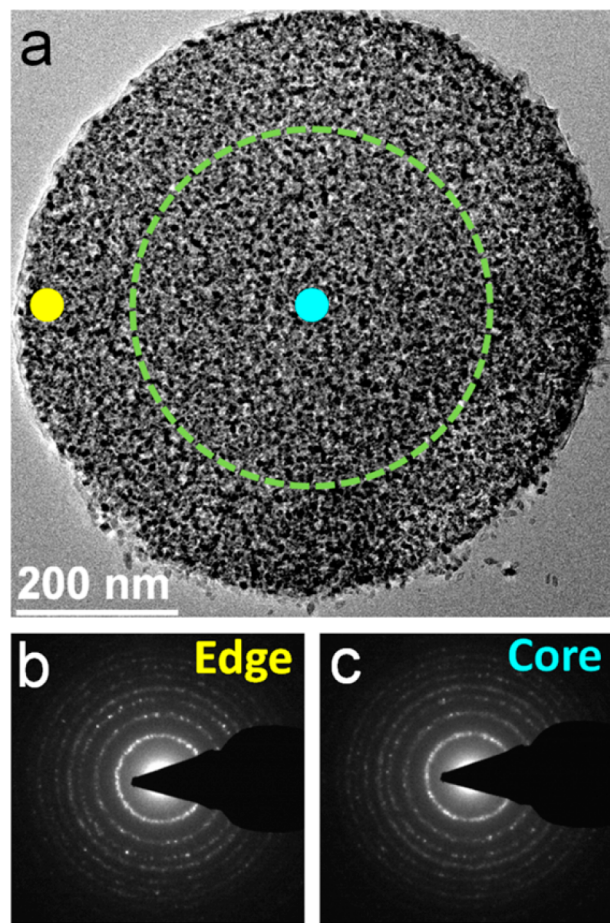


**Figure 3.** TEM image (a) of an ultramicrotomed cross section of a bead with 0.75 crystallization extent (determined by PXRD). The green dashed circle defines the crystalline/amorphous boundary assuming crystallization progresses from the edge toward the core (note that the diameter of the green circle is 0.63 of the diameter of the bead so that the volume within the green circle is 0.25 of the volume of the bead); this crystalline/amorphous boundary does not exist as confirmed by SAED, suggesting 3D crystallization. (b,c) SAED patterns of the edge (yellow circle) and core (blue circle) regions of the bead, respectively.

phase, and an amorphous/anatase phase boundary would be visible in Figure 3a.

Solid-state transformation is commonly responsible for 3D crystallization of nonporous solid materials, but given such low synthesis temperature and fast kinetics, solid state transformation is unlikely here. Also, if the crystallization follows the solid-state transformation mechanism, we would expect the same kinetics for the crystallization occurring when using  $\text{TiO}_2/\text{HDA}$  hybrid beads (PD01) and HDA-free  $\text{TiO}_2$  beads (PD05), which is not the case (Figure 2c). Hence, the crystallization involves the dissolution of the amorphous precursor and the nucleation and crystal growth of the crystalline anatase. Solvent-assisted 3D crystallization requires the penetration of solvent into the precursor beads that results in the contact of amorphous titania with water molecules within the entire beads, but how does the solvent enter the interior of the beads at the early stage given that the  $\text{TiO}_2/\text{HDA}$  hybrid precursor beads are nonporous? It may be due to the wormhole-like internal mesostructure of the beads consisting of amorphous  $\text{TiO}_2$  domains interconnected with the surrounding HDA molecules. The dissolution of HDA may be much faster than the crystallization of  $\text{TiO}_2$ , so that solvent can enter the interior after partial removal of HDA, and therefore, the crystallization occurs three-dimensionally. Here using an ethanol/water mixture as the solvent is very important. HDA can be readily wetted and dissolved by ethanol, thus ethanol molecules can bring water into the interior of the precursor beads. Water (even at low quantities) had a catalytic effect on the crystallization of amorphous  $\text{TiO}_2$  during hydrothermal synthesis,<sup>37,38</sup> triggering the 3D crystallization process. Note that HDA dissolution at this stage may also contribute to the induction period, apart from dissolution of amorphous  $\text{TiO}_2$  and nucleation of anatase. This proposal is in agreement with the kinetic results. Assuming the dissolution of HDA is faster than the crystallization of  $\text{TiO}_2$ , the overall crystallization rate should be controlled by the crystallization step. That is to say, the overall rate should be promoted by the water content (or decreasing ethanol concentration). This was observed from *in situ* PXRD kinetic curves (Figure 2d), which shows a gradual increase in the rate of crystallization with decreasing ethanol concentration from 91 to 67 vol %.

The crystallization involves the dissolution of the precursor, precipitation of anatase, and little to no mass transport of the dissolved species to the bulk solution outside of the beads. As the overall spherical morphology of the precursor beads is preserved in the anatase product beads, we propose that dissolution is the rate limiting step. If the anatase precipitation is relatively faster than dissolution, the dissolved Ti(IV) species can be precipitated locally before it is transported away to the bulk solvent. As a result, the overall spherical morphology is inherited. If anatase precipitation were the rate limiting step, then the dissolved Ti(IV) species may be transported to the bulk solution, and the nucleation and growth may also occur on the outer surface of the beads, resulting in epitaxial growth. This is the case for the reported crystallization of spiky anatase beads in solvents with very high ammonia concentration.<sup>30</sup> Under such conditions, the nucleation and growth is inhibited due to the complexing effect of ammonia that can interact with a large amount of dissolved Ti(IV) species. Therefore, the dissolved species are transported away from the dissolution site and nucleate and grow on the outer surface, resulting in spiky anatase beads with large elongated single crystal particles growing perpendicular to the outer surface of the beads.<sup>30</sup>

In spite of the relatively fast generation of a solvent pathway by the removal of HDA, the presence of HDA in the  $\text{TiO}_2/\text{HDA}$  hybrid precursor beads and in the local solvent may restrict water entrance to the amorphous  $\text{TiO}_2$  domains due to the hydrophobic nature of HDA and, as a result, may retard  $\text{TiO}_2$  crystallization. This is actually a very profound effect. *In situ* PXRD of the crystallization using precursor beads with and without HDA showed that the synthesis using an HDA-free precursor was about 5 times faster than the synthesis using a  $\text{TiO}_2/\text{HDA}$  hybrid precursor (Figure 2c). Note that the HDA-free precursor is highly porous (Figure S4 and Table S1, Supporting Information); hence, the solvent (water and ethanol) can quickly fill the entire bead and promote the hydrolysis of amorphous  $\text{TiO}_2$ , therefore resulting in a rapid crystallization process relative to the case when  $\text{TiO}_2/\text{HDA}$  hybrid precursor beads were used.

### 3.4. Synthesis Mechanism: Sequence of Nucleation and Crystal Growth.

WPPM analysis of the anatase crystal size distribution evolution as a function of time (Figures 4a and

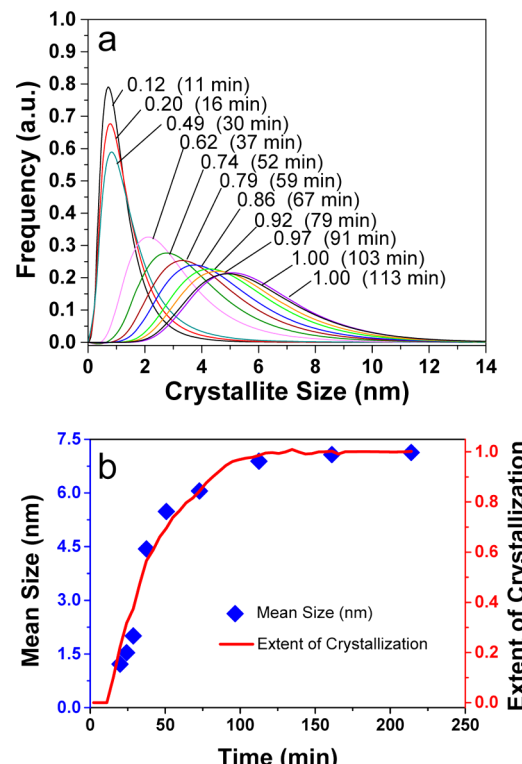


**Figure 4.** (a) Crystallite size distribution evolutions for PD02; the number before the bracket is the extent of crystallization, and in the bracket is the crystallization time (min) excluding induction time. Crystallite size distribution evolution for the other runs is provided in the Supporting Information (Figure S13). (b) A comparison of the mean crystal size and the extent of crystallization curve for PD02 showing a close correlation between these parameters.

S13, Supporting Information) indicates that for all 9 syntheses the size distributions were narrow (centered at ~1 nm) at the early stage of crystallization, became broader with time, and after a certain crystallization extent (0.68–0.85) the broadness remained relatively unchanged, while the crystallite size was still growing. However, after complete crystallization, both the size distribution and crystallite size stopped changing. This correlating relationship between crystallite size and extent of crystallization is highlighted in Figure 4b.

On the basis of the above results, we can propose the following 4-step nucleation and growth mechanism. (1) The dissolution of amorphous  $\text{TiO}_2$  makes the local solution supersaturated with respect to anatase and triggers initial nucleation; (2) anatase starts to grow and its crystallite size increases with time; but at this stage, nucleation is still continuing, leading to a broader size distribution; (3) when the crystallization extent reaches 0.68–0.85, nucleation stops, leaving only crystal growth until complete crystallization (exhaustion of the precursor); as a result, the shape of the size distribution does not change but the mean size continues to grow; and (4) after complete crystallization, no Ostwald ripening occurs resulting in the stabilized anatase crystallite size distribution. The size stabilization after complete crystallization is in agreement with a recent study for synthesizing anatase beads using laboratory autoclaves.<sup>6</sup>

Kinetic analysis can provide insight into reaction mechanisms. The kinetic analysis here was performed using the Avrami–Erofe’ev equation<sup>39,40</sup>

$$\alpha = 1 - \exp[-k^n(t - t_0)^n]$$

where  $\alpha$  is the reaction extent (in our case extent of crystallization),  $k$  is the rate constant,  $t$  is the reaction time,  $t_0$  is the induction time, and  $n$  is the Avrami exponent, which is related to the reaction mechanism. The Avrami–Erofe’ev method is very versatile in describing the nucleation and crystallization of materials, and indeed, it has been successfully applied in understanding the solvothermal synthesis of several materials including zeolite,<sup>25</sup> metal–organic framework,<sup>41</sup> and metal oxides and hydroxides.<sup>15,42–44</sup> The value of  $n$  and  $k$  can be conveniently obtained by applying the Sharp–Hancock plot,<sup>45</sup> which plots  $\ln[-\ln(1 - \alpha)]$  against  $\ln(t - t_0)$  and gives a straight line with a slope of  $n$  and an intercept of  $n \ln(k)$ . A change in the reaction mechanism can be identified by a change in the slope.

Figure 5a is an example of the Sharp–Hancock plots showing the effects of temperature on the crystallization. The corresponding  $n$  and  $k$  values for each synthesis are summarized in Table 1. In most cases,  $n$  was observed to change in the course of crystallization indicating a change in mechanism. A change in the  $n$  value during crystallization is not uncommon in material synthesis, e.g., a similar change was also observed in the supercritical synthesis of  $\text{TiO}_2$ .<sup>9</sup> The transition point for the change in  $n$  corresponds to the extent of crystallization range 0.68–0.90, in good agreement with the transition point from increasing size distribution broadness to stabilizing of the distribution broadness (Figure 4a). The  $n$  values for the syntheses before the transition are in the range 1–2, which may suggest a diffusion controlled growth with decreasing nucleation rate.<sup>44,46</sup> In our case, it suggests a diffusion controlled growth of anatase nanocrystals within the beads with decreasing nucleation rate. This again supports the proposed mechanism because, before the transition, the size of anatase nanocrystals continues growing accompanied by disappearing nucleation events. The  $n$  value after the transition varies greatly, from 0.77 to 2.82, which may indicate different growth models.

From the rate constant at three temperatures, the activation energy for the crystallization of PB(HDA)1150 in 67 vol % ethanol was obtained by plotting  $\ln(k)$  against  $1000/T$  following the Arrhenius equation

$$k = A \cdot \exp(-E_a/RT)$$

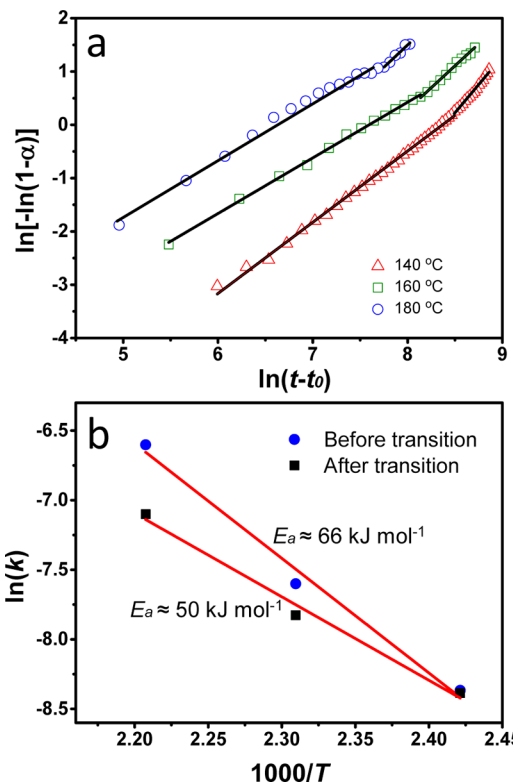


**Figure 5.** (a) Sharp–Hancock plots for PD01, PD02, and PD03 conducted at different temperatures, and (b) Arrhenius plots for before and after the transition.

where  $A$  is the pre-exponential factor,  $E_a$  the activation energy,  $R$  the gas constant, and  $T$  the absolute temperature. From the slope of the plot (Figure 5b), the activation energy for the solvothermal crystallization of the mesoporous  $\text{TiO}_2$  beads was calculated to be around 66 and 50  $\text{kJ mol}^{-1}$  before and after the transition of  $n$ , respectively. A similar value was also reported in the literature for the solvothermal synthesis of  $\text{TiO}_2$  (66  $\text{kJ mol}^{-1}$ ) although at much higher temperatures (300–550 °C) and pressures (25 MPa).<sup>9</sup> An activation energy in the range 22–84  $\text{kJ mol}^{-1}$  usually means a dissolution and precipitation mechanism,<sup>47</sup> suggesting anatase grows from the solution after the dissolution of amorphous  $\text{TiO}_2$ . The relatively low activation energy after the transition can be interpreted by the proposed mechanism. Before the transition, the nucleation contributes to the high activation energy. After the transition, there is only crystal growth, and as new anatase grows epitaxially on the facets of existing anatase nanocrystals, a lower energy barrier needs to be overcome.

**3.5. In Situ SAXS.** To complement the in situ PXRD data, three in situ SAXS experiments were also carried out, under conditions identical to three in situ PXRD experiments: the conditions for S01, S02, and S03 were equivalent to PD02, PD03, and PD04, respectively. The time evolutions of the SAXS curve profiles are very similar for all three experiments (Figure S3, Supporting Information), indicating the same crystallization mechanism dominated for the solvothermal crystallization using large (S01) and small (S03) precursor beads, and at different temperatures (160 and 180 °C for S01 and S02). Figure 6a shows SAXS curves for S01 (160 °C using 1150 nm precursor beads). The detailed procedure for data analysis is provided in the Supporting Information.

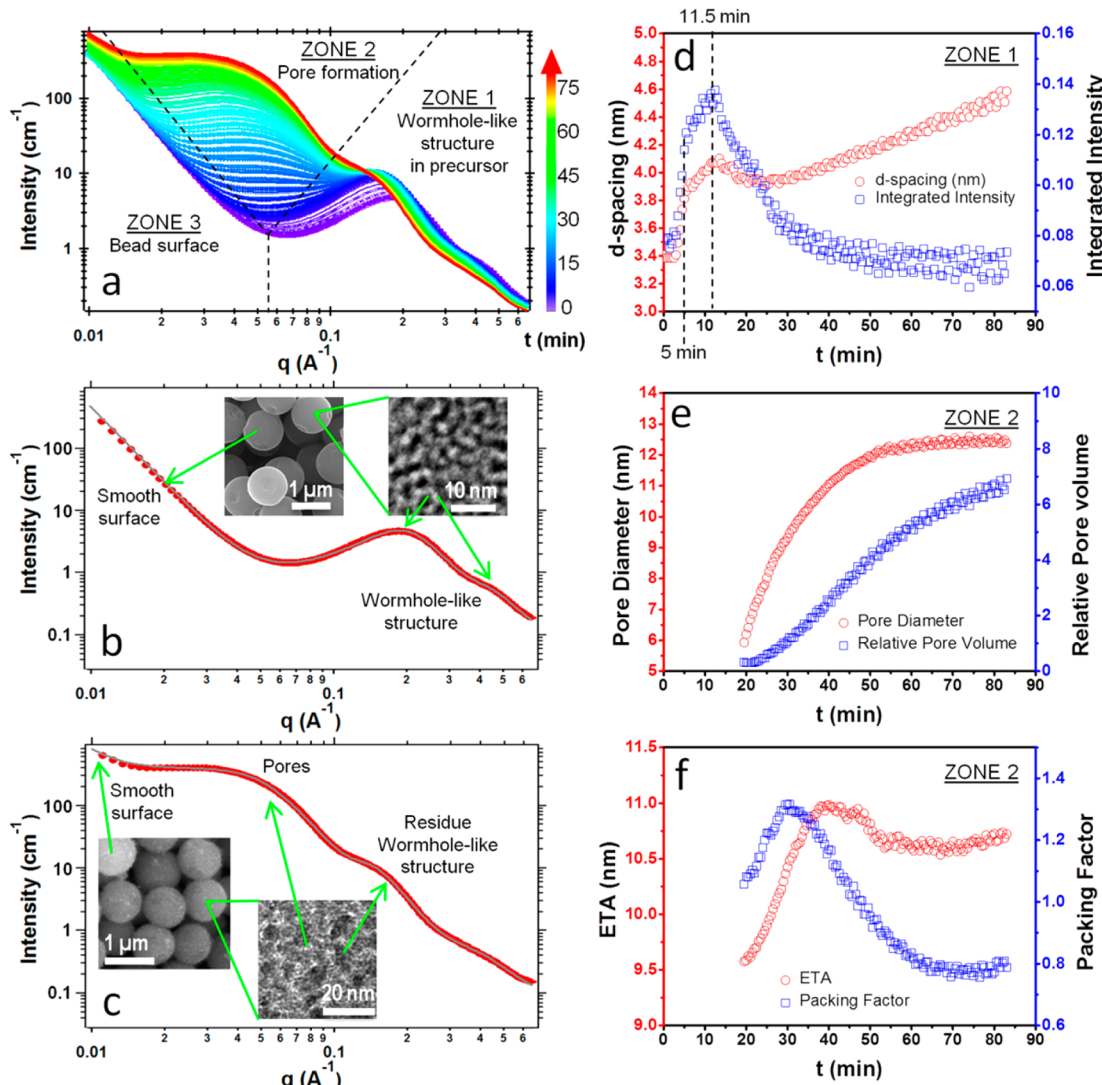


**Figure 6.** In situ SAXS results for S01. (a) Time evolution of SAXS curves that can be divided into three zones; (b) SAXS curve for the precursor beads showing a Porod scattering region from the smooth bead surface and 2 broad peaks from the wormhole-like mesostructure; (c) SAXS curve for the product beads showing a Porod scattering tail from the bead surface, a mid  $q$  scattering region from the newly formed pores, and a residue broad peak at high  $q$  from the residue wormhole-like mesostructure; (d) the evolution of  $d$  spacing and integrated intensity for the peak centered at around  $0.19 \text{ \AA}^{-1}$ ; (e) the pore diameter and volume evolution of the newly formed pores; and (f) time evolution of average center-to-center distance (ETA) of neighboring pores and average number of neighboring pores (packing factor).

At the beginning of the synthesis, the scattering curve for the precursor beads (Figure 6b) has two broad small angle diffraction peaks at high  $q$ , with the peak positions at around  $0.19$  and  $0.39 \text{ \AA}^{-1}$  (Zone 1 in Figure 6a). These peaks reflect the interface distances of the wormhole-like internal mesostructure of the precursor beads (Figure 6b). The  $d$  spacing for the peak at  $0.19 \text{ \AA}^{-1}$  ( $3.5 \text{ nm}$ ) is about twice the  $d$  spacing of the peak at  $0.39 \text{ \AA}^{-1}$  ( $1.6 \text{ nm}$ ), suggesting the peak at  $0.39 \text{ \AA}^{-1}$  may be a second order of the peak at  $0.19 \text{ \AA}^{-1}$ . The  $d$ -spacing value for the peak at  $0.19 \text{ \AA}^{-1}$  is in good agreement with the previously reported value for the same material but measured by small angle XRD.<sup>23</sup> However, the earlier study did not observe the second order peak, probably due to the relative low-resolution of small-angle XRD compared with synchrotron SAXS. The low  $q$  region shows a power-law behavior (linear on the log-scale), representing extended Porod scattering from the smooth surface of the beads (Figure 6b and Zone 3 in Figure 6a).<sup>48</sup>

Upon heating, the  $d$  spacing of the main diffraction peak ( $q = 0.19 \text{ \AA}^{-1}$ ; Figure 6a) first increased rapidly from  $3.5$  to  $3.9 \text{ nm}$  (Figure 6d) in the first  $5 \text{ min}$ , and then further increased slightly to  $4.1 \text{ nm}$  until  $11.5 \text{ min}$ , suggesting some expansion of the wormhole-like mesostructure. This expansion may be due to the solvent entrance into the bead interior after fast partial dissolution of HDA at the  $\text{TiO}_2/\text{HDA}$  phase interface or the growth of the  $\text{TiO}_2$  crystals that is accompanied by reorganization of the matter and of the HDA in larger domains. The rapid increase in the first  $5 \text{ min}$  is probably due to a combined effect from solvent entrance as well as thermal expansion because it took about  $4.5 \text{ min}$  to raise the temperature to  $160^\circ\text{C}$ , and after that, the temperature was stabilized at  $160^\circ\text{C}$ .

The  $d$ -spacing expansion was initially accompanied by an increase in integrated intensity (Figure 6d). This may suggest the increase in scattering contrast due to the change in interface chemistry as a result of the dissolution of HDA and the entrance of the ethanol/water solvent. It is also possible that

the wormhole-like internal network is becoming more uniform in size when heated. This size uniformity reflects the initial dissolution of HDA along the  $\text{TiO}_2/\text{HDA}$  interface, allowing the wormhole-like mesostructure to reorganize to a higher uniformity. However, after 11.5 min, which coincides with the onset time of crystallization from *in situ* PXRD results (Table 1 and Figure 2b), the integrated intensity decreased continually, suggesting the crystallization of anatase occurred at the expense of the uniformity of the wormhole-like mesostructure (on dissolution of the amorphous  $\text{TiO}_2$ ). The  $d$  spacing of the peak also had a transition at 11.5 min, first decreasing then increasing gradually until the end of the synthesis.

After the onset of crystallization at 11.5 min, a new region at intermediate  $q$  range (Zone 2 in Figure 6a) became apparent. This zone suggests the growth of new pores (space between crystallites) as a result of the growth of anatase crystallites (Figure 6c). The SAXS curve for the product beads also show a Porod scattering tail for the product bead surface at high  $q$ , and a broad peak at high  $q$  from the residue wormhole-like mesostructure (note that the synthesis did not reach completion due to limited beam time). By Guinier analysis,<sup>48</sup> assuming hard sphere structural interferences, the time evolution of pore diameter ( $D = 3.33R_g$ , where  $R_g$  is radius of gyration), relative pore volume (the  $G$  parameter in the Guinier equation), center-to-center neighbor pore distance (ETA), and packing factor phi (average neighboring pores) can be determined. The time evolution of these parameters (Figure 6e,f) show the following:

- (1) The pore size first rapidly increases with time from 6 to 12 nm and then increases very slowly after 50 min synthesis. This is in agreement with the growth rate trend for anatase, which has a transition point when the extent of crystallization is ~0.70 (50 min, Figure 4a). Because the newly formed pores are due to interstitial space among the solid domains including amorphous  $\text{TiO}_2$  precursor and the newly formed anatase nanocrystals, and also because anatase nanocrystals are larger than the amorphous  $\text{TiO}_2$  domains, the growth of anatase at the expense of amorphous  $\text{TiO}_2$  domains will increase the size of the pores. However, after the transition point, although the anatase mean crystal size is still increasing (Figure 4a), the growing small crystals can occupy the pores; hence, the pore size increases only slowly.
- (2) The increasing pore volume with time also indicates the growth of anatase crystallites. Initially the amorphous precursor beads are nonporous with a wormhole-like mesostructure. The continued dissolution of HDA and the crystallization from amorphous  $\text{TiO}_2$  to anatase nanocrystals generate increased pore volume.
- (3) The center-to-center neighboring pore distance first increases with time from 9.5 to 11 nm, but after 37 min, it decreases slightly to 10.7 nm. This may indicate that first both pores and crystallites grow and then the crystallites are packed more closely.
- (4) The average neighboring pore numbers first increase with time and then decrease continuously after 30 min synthesis. This indicates that after 30 min the mesoporous structure becomes less ordered, even though it is more packed.

## 4. CONCLUSIONS

Using synchrotron *in situ* PXRD and SAXS the solvothermal crystallization of submicrometer-sized mesoporous anatase beads was shown to be a 3-dimensional crystallization process involving 4-steps. This process involves (1) an induction period for HDA (organic structure-directing agent) and amorphous  $\text{TiO}_2$  dissolution, (2) anatase nucleation and growth at the expense of precursor dissolution, (3) coarsening in anatase crystals accompanied by continued precursor dissolution, and (4) reaching stable crystallite size with no significant Ostwald ripening. The understanding of this synthesis has several important implications. First, the synthesis rate is promoted by increasing temperature or water content or using a porous amorphous precursor free from HDA; rapid and large scale synthesis protocols may be designed by rationally adjusting these parameters. Second, because the crystallization rate is insensitive to the size of the beads as it is a 3D crystallization mechanism, varying bead sizes may be synthesized without affecting the crystallization rate; this gives flexibility for various applications requiring different sizes of materials. Third, the broad size distribution of the anatase crystallites is due to concurrent nucleation and growth at the early stage of crystallization; thus, to have a narrower size distribution, conditions that can separate nucleation from growth would be required. Finally, because Ostwald ripening is not significant, control of the mean crystallite size is not by prolonged synthesis time but rather by the control of nucleation. This is because a high nucleation energy barrier results in the formation of a limited number of nuclei, thus leaving sufficient precursor for the growth stage, which eventually forms large crystallites. On the contrary, a low nucleation energy barrier results in the formation of a greater number of nuclei at the beginning of the synthesis, preventing them from growing to large crystallites due to the exhaustion of the available precursor. The control of nucleation may be achieved by introducing complexing agents to the solvothermal process, such as ammonia, which can increase the nucleation energy barrier and hence produce larger crystallites.

## ■ ASSOCIATED CONTENT

### S Supporting Information

Details of the Rietveld analysis of powder diffraction data, whole powder pattern modeling, SAXS data analysis, SAXS curves for S01, S02, and S03 experiments, physical properties of the precursor beads, *in situ* PXRD patterns for PD01 and PD03-09, crystallite size distribution evolution for PD01 and PD03-09. This material is available free of charge via the Internet at <http://pubs.acs.org>.

## ■ AUTHOR INFORMATION

### Corresponding Author

\*(R.A.C.) E-mail: rcaruso@unimelb.edu.au.

### Notes

The authors declare no competing financial interest.

## ■ ACKNOWLEDGMENTS

The CSIRO Office of the Chief Executive (OCE) Postdoctoral and Science Leader Schemes are acknowledged for financial support. This research was undertaken on the powder diffraction and small- and wide-angle X-ray scattering beamlines at the Australian Synchrotron, Victoria, Australia (beam time awards AS113/PD/4160 and AS131/SAXSFI/5984), through

the Science and Industry Endowment Fund Special Research Program—Synchrotron Science. The authors wish to thank Dr. Wei Li, Dr. Nathan Webster, Dr. Xingdong Wang, Mr. Jingchao Song, Mr. Zaiquan Xu, Dr. Justin Kimpton, Dr. Stephen Mudie, and Dr. Nigel Kirby for assistance with synchrotron data collection. R.A.C. acknowledges the Australian Research Council for a Future Fellowship (FT0990583). Dr. Simon Crawford is thanked for ultramicrotoming samples in preparation for TEM characterization. The Melbourne Advanced Microscopy Facility at The University of Melbourne is acknowledged for electron microscopy access.

## ■ REFERENCES

- (1) Chen, X.; Mao, S. S. *Chem. Rev.* **2007**, *107*, 2891.
- (2) Yang, H. G.; Sun, C. H.; Qiao, S. Z.; Zou, J.; Liu, G.; Smith, S. C.; Cheng, H. M.; Lu, G. Q. *Nature* **2008**, *453*, 638.
- (3) Zhao, Z.; Sun, Z.; Zhao, H.; Zheng, M.; Du, P.; Zhao, J.; Fan, H. *J. Mater. Chem.* **2012**, *22*, 21965.
- (4) Liao, J. Y.; Lei, B. X.; Kuang, D. B.; Su, C. Y. *Energy Environ. Sci.* **2011**, *4*, 4079.
- (5) Wang, X. D.; Dornom, T.; Blackford, M.; Caruso, R. A. *J. Mater. Chem.* **2012**, *22*, 11701.
- (6) Cao, L.; Chen, D.; Caruso, R. A. *Angew. Chem., Int. Ed.* **2013**, *52*, 10986.
- (7) Hummer, D. R.; Heaney, P. J.; Post, J. E. *J. Cryst. Growth* **2012**, *344*, 51.
- (8) Jensen, H.; Bremholm, M.; Nielsen, R. P.; Joensen, K. D.; Pedersen, J. S.; Birkedal, H.; Chen, Y. S.; Almer, J.; Sogaard, E. G.; Iversen, S. B.; Iversen, B. B. *Angew. Chem., Int. Ed.* **2007**, *46*, 1113.
- (9) Eltzholz, J. R.; Tyrsted, C.; Jensen, K. M. O.; Bremholm, M.; Christensen, M.; Becker-Christensen, J.; Iversen, B. B. *Nanoscale* **2013**, *5*, 2372.
- (10) Mi, J. L.; Clausen, C.; Bremholm, M.; Lock, N.; Jensen, K. M. O.; Christensen, M.; Iversen, B. B. *Cryst. Growth Des.* **2012**, *12*, 6092.
- (11) Jensen, K. M. O.; Christensen, M.; Juhas, P.; Tyrsted, C.; Bojesen, E. D.; Lock, N.; Billinge, S. J. L.; Iversen, B. B. *J. Am. Chem. Soc.* **2012**, *134*, 6785.
- (12) Tyrsted, C.; Jensen, K. M. O.; Bojesen, E. D.; Lock, N.; Christensen, M.; Billinge, S. J. L.; Iversen, B. B. *Angew. Chem., Int. Ed.* **2012**, *51*, 9030.
- (13) Bremholm, M.; Felicissimo, M.; Iversen, B. B. *Angew. Chem., Int. Ed.* **2009**, *48*, 4788.
- (14) Du, Y.; Ok, K. M.; O'Hare, D. *J. Mater. Chem.* **2008**, *18*, 4450.
- (15) Williams, G. R.; Norquist, A. J.; O'Hare, D. *Chem. Mater.* **2006**, *18*, 3801.
- (16) de Moor, P.; Beelen, T. P. M.; van Santen, R. A. *J. Phys. Chem. B* **1999**, *103*, 1639.
- (17) Walton, R. I.; Millange, F.; O'Hare, D.; Davies, A. T.; Sankar, G.; Catlow, C. R. A. *J. Phys. Chem. B* **2001**, *105*, 83.
- (18) Norby, P. *Curr. Opin. Colloid Interface Sci.* **2006**, *11*, 118.
- (19) Brand, H. E. A.; Scarlett, N. V. Y.; Grey, I. E. *J. Appl. Crystallogr.* **2012**, *45*, 535.
- (20) Scarlett, N. V. Y.; Grey, I. E.; Brand, H. E. A. *J. Synchrotron Radiat.* **2013**, *20*, 366.
- (21) Brand, H. E. A.; Scarlett, N. V. Y.; Grey, I. E.; Knott, R. B.; Kirby, N. *J. Synchrotron Radiat.* **2013**, *20*, 626.
- (22) Chen, D. H.; Huang, F. Z.; Cheng, Y. B.; Caruso, R. A. *Adv. Mater.* **2009**, *21*, 2206.
- (23) Chen, D. H.; Cao, L.; Huang, F. Z.; Imperia, P.; Cheng, Y. B.; Caruso, R. A. *J. Am. Chem. Soc.* **2010**, *132*, 4438.
- (24) Wang, X.; Cao, L.; Chen, D.; Caruso, R. A. *ACS Appl. Mater. Interfaces* **2013**, *5*, 9421.
- (25) Norby, P. *J. Am. Chem. Soc.* **1997**, *119*, 5215.
- (26) Schmitt, B.; Bronnimann, C.; Eikenberry, E. F.; Gozzo, F.; Hormann, C.; Horisberger, R.; Patterson, B. *Nucl. Instrum. Methods Phys. Res., Sect. A* **2003**, *501*, 267.
- (27) Scardi, P.; Leoni, M. *Acta Crystallogr., Sect. A: Found. Crystallogr.* **2002**, *58*, 190.
- (28) Leoni, M.; Confente, T.; Scardi, P. Z. *Kristallogr.* **2006**, *23*, 249.
- (29) Ilavsky, J.; Jemian, P. R. *J. Appl. Crystallogr.* **2009**, *42*, 347.
- (30) Chen, D. H.; Huang, F. Z.; Cao, L.; Cheng, Y. B.; Caruso, R. A. *Chem.—Eur. J.* **2012**, *18*, 13762.
- (31) Reboul, J.; Furukawa, S.; Horike, N.; Tsotslas, M.; Hirai, K.; Uehara, H.; Kondo, M.; Louvain, N.; Sakata, O.; Kitagawa, S. *Nat. Mater.* **2012**, *11*, 717.
- (32) Xia, F.; Brugger, J.; Chen, G. R.; Ngothai, Y.; O'Neill, B.; Putnis, A.; Pring, A. *Geochim. Cosmochim. Acta* **2009**, *73*, 1945.
- (33) Xia, F.; Zhou, J. W.; Brugger, J.; Ngothai, Y.; O'Neill, B.; Chen, G. R.; Pring, A. *Chem. Mater.* **2008**, *20*, 2809.
- (34) Xia, F.; Brugger, J.; Ngothai, Y.; O'Neill, B.; Chen, G. R.; Pring, A. *Cryst. Growth Des.* **2009**, *9*, 4902.
- (35) Anderson, M. W.; Holmes, S. M.; Hanif, N.; Cundy, C. S. *Angew. Chem., Int. Ed.* **2000**, *39*, 2707.
- (36) Qian, G. J.; Xia, F.; Brugger, J.; Skinner, W. M.; Bei, J. F.; Cren, G. R.; Pring, A. *Am. Mineral.* **2011**, *96*, 1878.
- (37) Yanagisawa, K.; Ovenstone, J. *J. Phys. Chem. B* **1999**, *103*, 7781.
- (38) Yanagisawa, K.; Yamamoto, Y.; Feng, Q.; Yamasaki, N. *J. Mater. Res.* **1998**, *13*, 825.
- (39) Avrami, M. *J. Chem. Phys.* **1939**, *7*, 1103.
- (40) Khanna, Y. P.; Taylor, T. *J. Polym. Eng. Sci.* **1988**, *28*, 1042.
- (41) Cravillon, J.; Schroder, C. A.; Bux, H.; Rothkirch, A.; Caro, J.; Wiebcke, M. *CrystEngComm* **2012**, *14*, 492.
- (42) Lupo, F.; Cockcroft, J. K.; Barnes, P.; Stukas, P.; Vickers, M.; Norman, C.; Bradshaw, H. *Phys. Chem. Chem. Phys.* **2004**, *6*, 1837.
- (43) Beale, A. M.; Sankar, G. *Chem. Mater.* **2003**, *15*, 146.
- (44) Fogg, A. M.; Price, S. J.; Francis, R. J.; O'Brien, S.; O'Hare, D. *J. Mater. Chem.* **2000**, *10*, 2355.
- (45) Hancock, J. D.; Sharp, J. H. *J. Am. Ceram. Soc.* **1972**, *55*, 74.
- (46) Hulbert, S. F. *J. Br. Ceram. Soc.* **1969**, *6*, 11.
- (47) Lasaga, A. C. *Kinetic Theory in the Earth Sciences*; Princeton University Press: Princeton, NJ, 1998.
- (48) Guinier, A.; Fournet, G. *Small-Angle Scattering of X-rays*; John Wiley & Sons, Inc.: New York, 1955.

# Supporting Information

## Understanding Solvothermal Crystallization of Mesoporous Anatase Beads by *In Situ* Synchrotron PXRD and SAXS

Fang Xia,<sup>†,‡</sup> Dehong Chen,<sup>§</sup> Nicola V. Y. Scarlett,<sup>‡</sup> Ian C. Madsen,<sup>‡</sup> Deborah Lau,<sup>†</sup> Matteo Leoni,<sup>||</sup> Jan Ilavsky,<sup>†</sup> Helen E. A. Brand,<sup>‡,§</sup> and Rachel A. Caruso,<sup>\*,†,§</sup>

<sup>†</sup>CSIRO Materials Science and Engineering, Clayton, VIC 3168, Australia

<sup>‡</sup>CSIRO Process Science and Engineering, Clayton, VIC 3168, Australia

<sup>§</sup>Particulate Fluids Processing Centre, School of Chemistry, The University of Melbourne, Melbourne, VIC 3010, Australia

<sup>||</sup>Department of Civil, Environmental and Mechanical Engineering, University of Trento, 38123 via Mesiano 77, Trento, Italy

<sup>†</sup>Advanced Photon Source, Argonne National Laboratory, 9700 S. Cass Avenue, Argonne, IL, USA

<sup>\*</sup>Australian Synchrotron, 800 Blackburn Rd., Clayton, VIC 3168, Australia

### 1. Rietveld analysis of PXRD patterns

The Rietveld refinement was carried out using the software TOPAS v4.2 (Bruker AXS) for determining the extent of crystallization. In the least square fitting, the 2-theta range below 5° was not used to avoid complication from rising background intensity due to small angle scattering, so the data range 5-80° was used. The refinements were run in batches where the output file from one refinement became the input file for the next dataset in the sequence. This approach minimizes the required parameter adjustment in the following dataset refinement hence minimizes the errors arising from inter correlated parameters. To improve the accuracy, the batch refinements were run backwards, starting with the last dataset when crystallization was complete. In the refinements, the background was modeled using a 5<sup>th</sup> order polynomial function. The amorphous peak arising from glass capillary, solvent, and amorphous starting precursor was modeled with a split pseudo-Voigt function. The zero error was obtained by refining the LaB<sub>6</sub> standard (NIST SRM 6606) and was then fixed for the sample datasets. The Lorentz-polarization factor was fixed to 90. The peaks were modeled by the pseudo-Voigt model and the instrumental peak profile parameters (*U*, *V*, *W*) were obtained by modeling of the LaB<sub>6</sub> standard. These peak

profile parameters were kept constant in the refinement of  $\text{TiO}_2$  samples and the peak broadening was modeled by crystallite size effects only. The tetragonal anatase starting crystal structure model was from the ICSD database (#63711). The unit cell parameters ( $a$ ,  $b$ ,  $c$ ), scale, thermal parameters, and peak broadening due to crystallite size effects were allowed to freely refine during the least-square fitting. The extent of crystallization of a dataset was calculated as the ratio between the scale factor of that dataset to the scale factor of the dataset after complete crystallization.

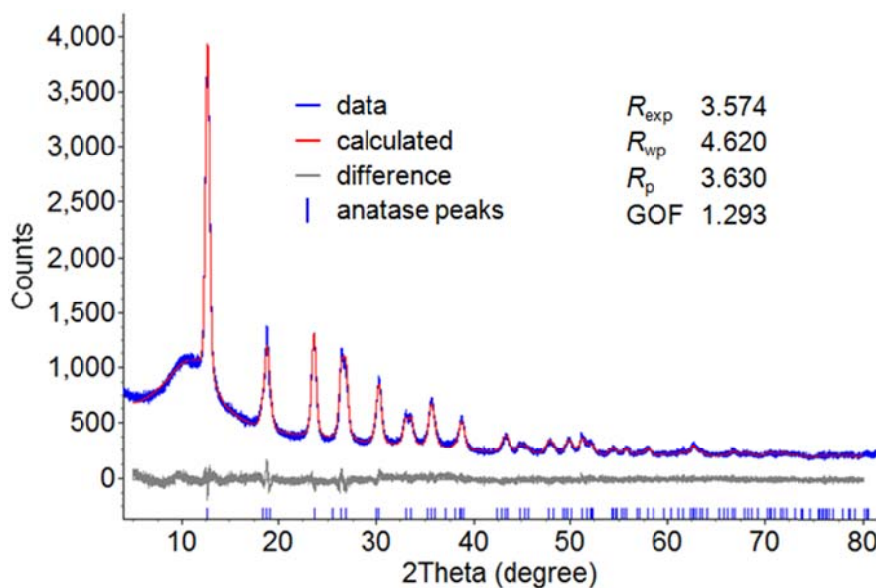


**Figure S1** An example of the Rietveld fitting (to the last PXTD pattern of PD02).  $R_{\text{exp}}$  - statistically expected R value;  $R_{\text{wp}}$  - weighted profile R value;  $R_{\text{p}}$  - profile R value; GOF - goodness of fit.

## 2. Whole Powder Pattern Modeling (WPPM)

For extracting the crystallite size distributions, WPPM analysis<sup>1</sup> was carried out using the software PM2K v1.68<sup>2</sup>. The WPPM is a least square fitting process analogous to the Rietveld method, but where the shape of the diffraction peak profiles is based on physical models for the microstructure (e.g. shape and size distribution of the crystallites, type and quantity of defects). In the analysis, octahedral domains were assumed (in agreement with TEM observations) dispersed according to a lognormal size distribution. The crystallites (or coherently scattering domains) correspond to the smallest crystalline regions inside the material. The background was modeled using a 4<sup>th</sup> order Chebyshev polynomial function and the amorphous peak due to the capillary

and solvent was modeled with a pseudo-Voigt function. In the fitting, 2-theta data range 5-58° was used, covering the major peaks of anatase. Peak profile fitting again used the pseudo-Voigt model and the instrumental peak profile parameters ( $U$ ,  $V$ ,  $W$ ,  $a$ ,  $b$ ) obtained from the standard LaB<sub>6</sub> powder (NIST SRM 660b). A typical fitting result is shown in Figure S2. For clarity, only selected distribution curves at various stages of synthesis are shown for each synthesis condition.

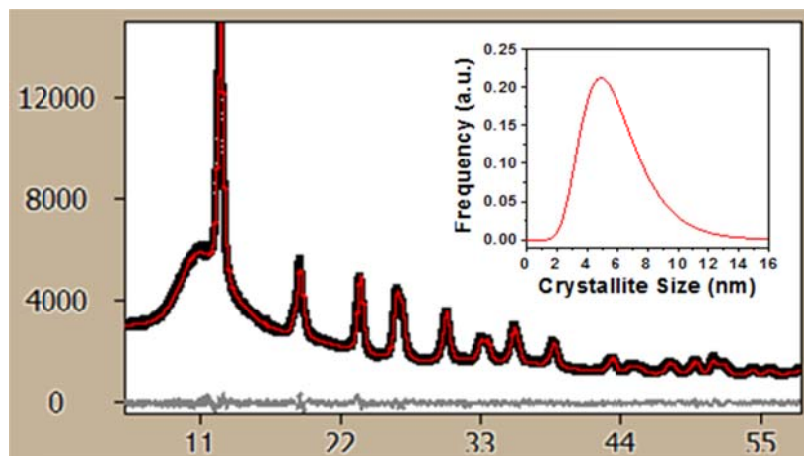


**Figure S2** An example of the WPPM fitting (to the last PXRD pattern of PD02) and the resulting size distribution for the completely crystallized sample.

### 3. Small Angle X-Ray Scattering (SAXS) Analysis

SAXS data was reduced using scatterBrain v1.730 (Australian Synchrotron), and analyzed by the software package Irena<sup>3</sup>. The starting precursor scattering curve consists of power-law scattering from the smooth surface of the beads at low  $q$  and the diffraction from internal wormhole-like structure at high  $q$  (Fig. S3). During the synthesis, scattering of the newly formed pores in the mid- $q$  continued to grow obscuring the Porod region for the scattering from the smooth beads surface at low  $q$ , while the scattering from the wormhole-like structure gradually decreased at high  $q$ . As a consequence, at the end of the synthesis, the product beads curve consists of (1) the surface scattering from the bead surface at low  $q$ , (2) the scattering from newly formed pores in the middle  $q$ , and (3) the residue wormhole-like structure (note that this synthesis had not completed crystallization due to limited beam time) at high  $q$ . From the above features, our fitting strategy was to do batch fitting starting from the final dataset and was running backwards towards the initial dataset. We used the “Modeling II” tool in the Irena package to model the three  $q$  regions.

- (1) Since from SEM we observe smooth beads surface, hence the low q region was modeled by using the Porod law to account for scattering from the smooth surface of the beads.
- (2) The middle q range was modeled by Unified fit (a combined Porod and Guinier fit)<sup>4</sup>. Here we are interested in the parameters  $R_g$  and G from Guinier fit. From  $R_g$  we can calculate pore diameter ( $d=3.33R_g$  for sphere) and because G is proportional to pore volume we can use it as the trend for pore volume change. An interference-based structure factor was also used in the fitting where the parameter ETA represents the center-to-center distance of neighboring pores and Phi represents the average number of neighboring pores.
- (3) The high q region was modeled by two diffraction peaks.

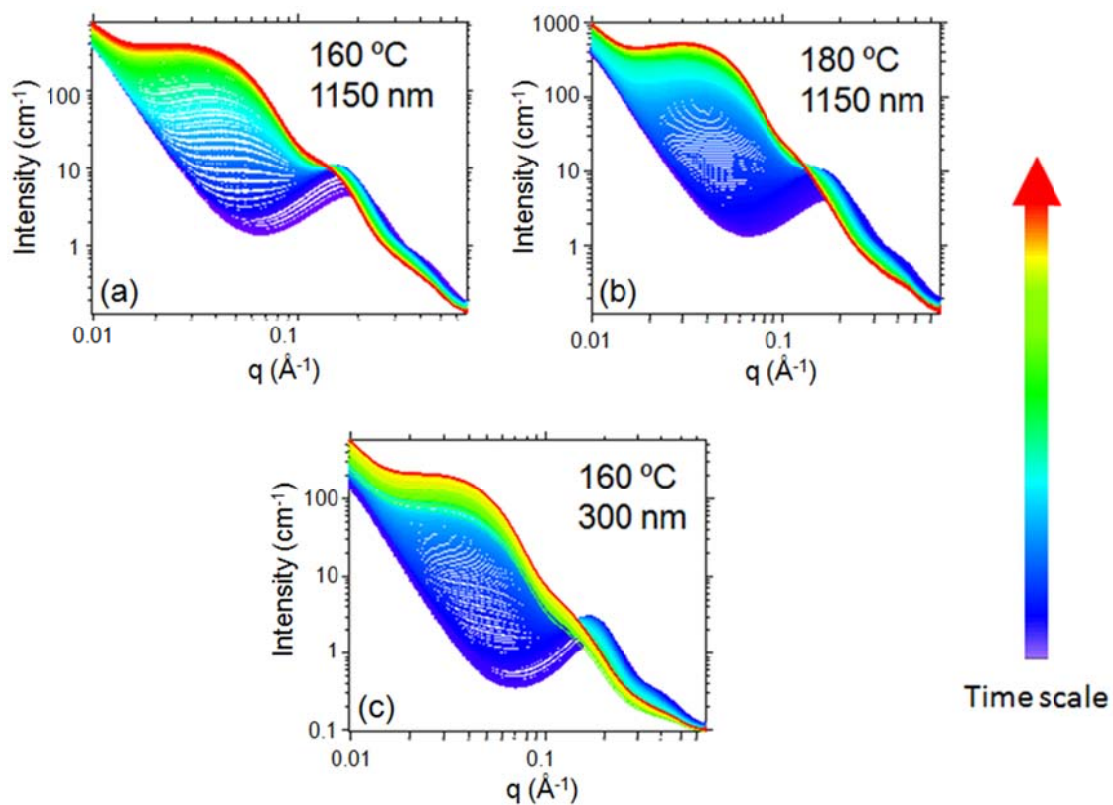


**Figure S3** SAXS curves for the three *in situ* syntheses of (a) S01, (b) S02, and (c) S03, showing similar change of the curves with synthesis time.

#### 4. Physical properties of precursor beads

Nitrogen gas sorption isotherms were measured at -196 °C by the volumetric method on a Micromeritics Tristar 3000 surface area and porosity analyzer. Prior to the measurement, precursor beads were evacuated at 80 °C for 18 h on a vacuum line (less than 30 mTorr). The standard multipoint Brunauer-Emmett-Teller (BET) method was utilized to calculate the specific surface area using the adsorption data in the  $P/P_0$  range from 0.05 to 0.20. The pore size distributions of the precursor beads were derived from the adsorption branches of the isotherms on the basis of a non-localized density functional theory (NLDFT) method.

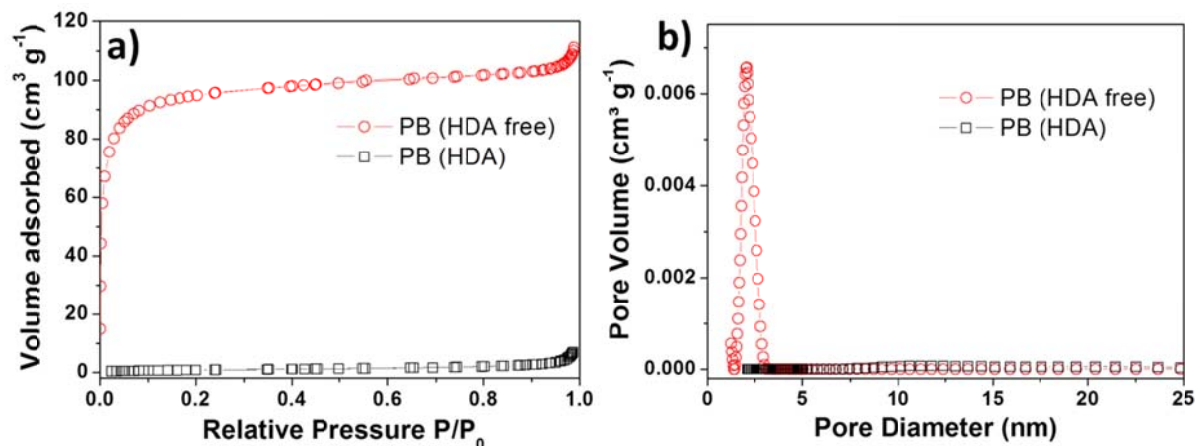


**Figure S4** (a) Nitrogen gas sorption isotherms and (b) pore size distribution of the amorphous precursor beads prepared in the absence of HDA (PB HDA free) and those in the presence of HDA (PB HDA).

**Table S1** Physical properties of the amorphous precursor beads prepared in the absence/presence of HDA.

Sample name	Surface area (m² g⁻¹)	Pore diameter (nm)	Pore volume (cm³ g⁻¹)
PB (HDA free)	367	2.1	0.167
PB (HDA)	3.3	Nonporous	0.009

## 5. Other experimental data

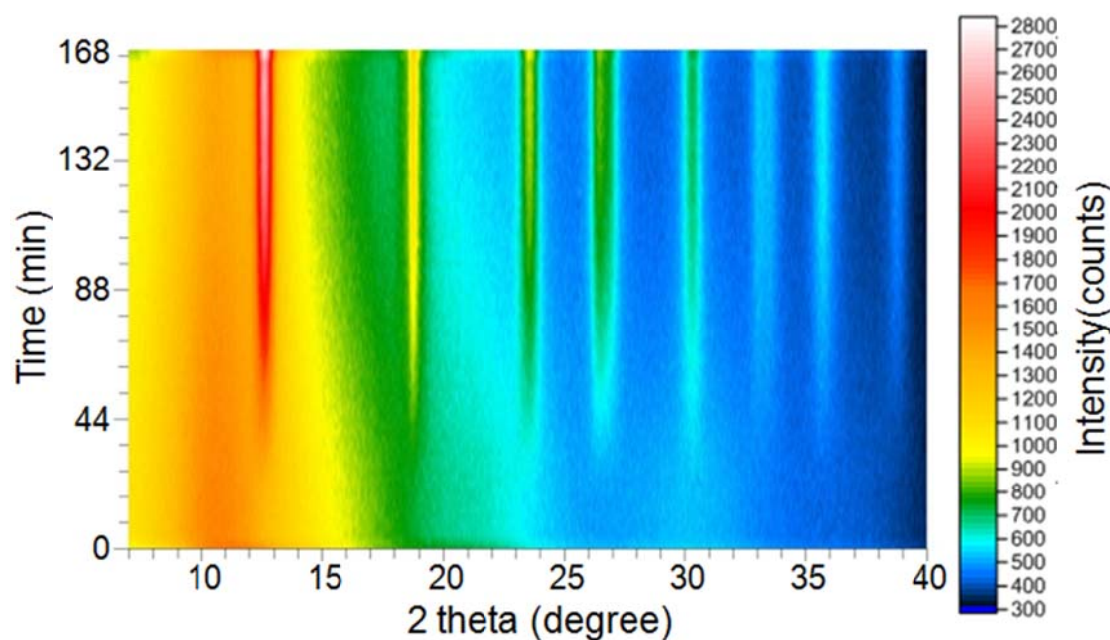


**Figure S5** Time evolution of *in situ* PXRD patterns (viewed down the intensity axis) for PD01 – crystallization of bicontinuous TiO<sub>2</sub>/HDA hybrid beads of 1150 nm diameter in 67 vol% ethanol at 140 °C.

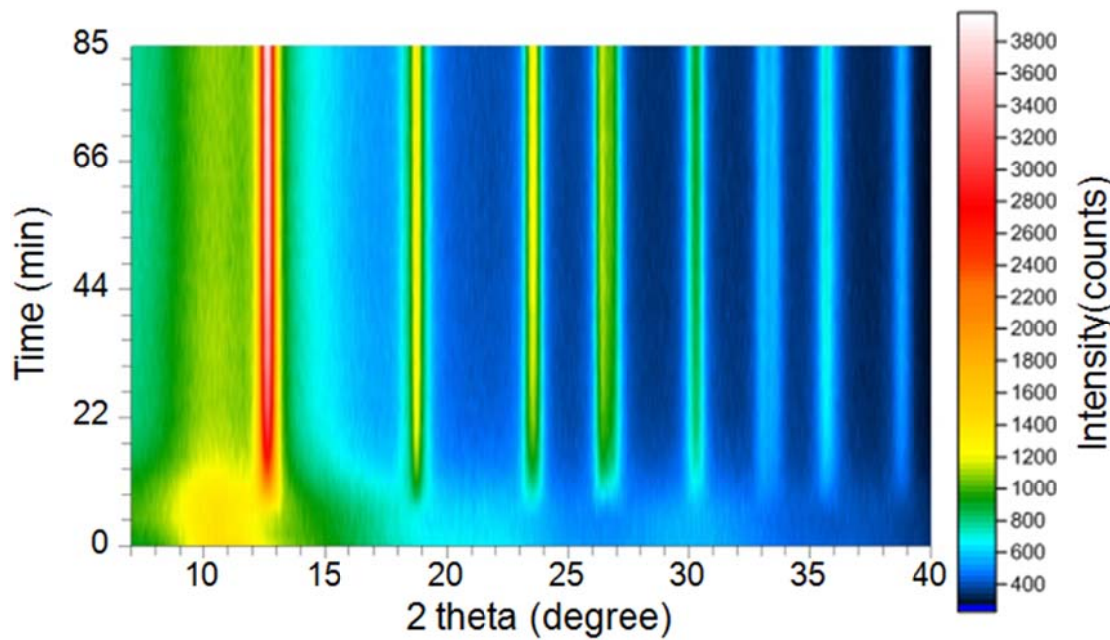


**Figure S6** Time evolution of *in situ* PXRD patterns (viewed down the intensity axis) for PD03 – crystallization of bicontinuous TiO<sub>2</sub>/HDA hybrid beads of 1150 nm diameter in 67 vol% ethanol at 180 °C.

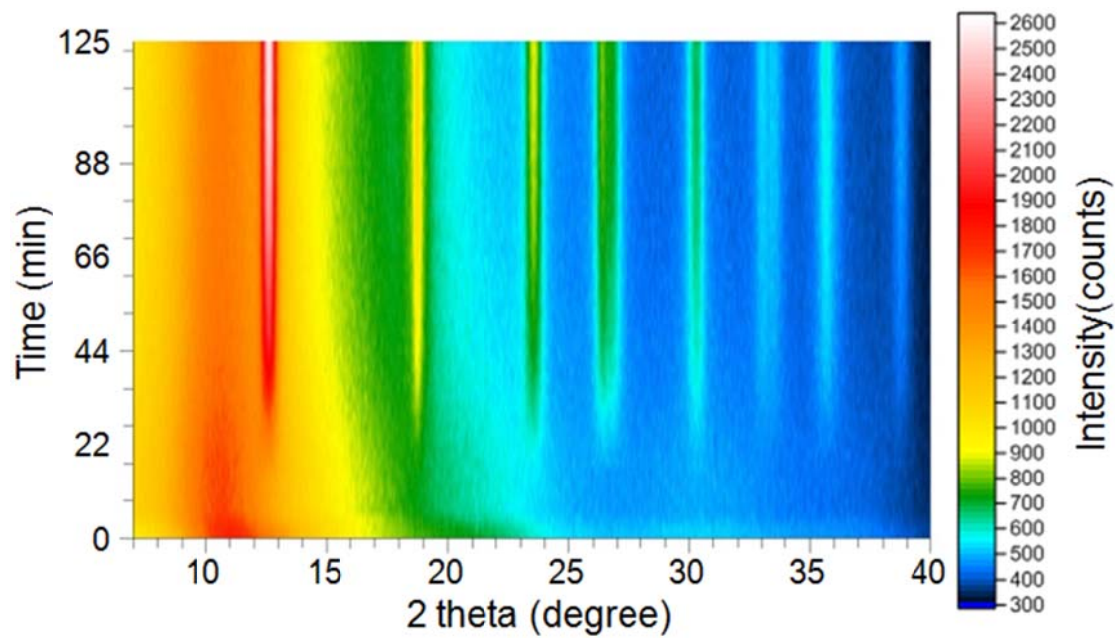


**Figure S7** Time evolution of *in situ* PXRD patterns (viewed down the intensity axis) for PD04 – crystallization of bicontinuous TiO<sub>2</sub>/HDA hybrid beads of 300 nm diameter in 67 vol% ethanol at 160 °C.

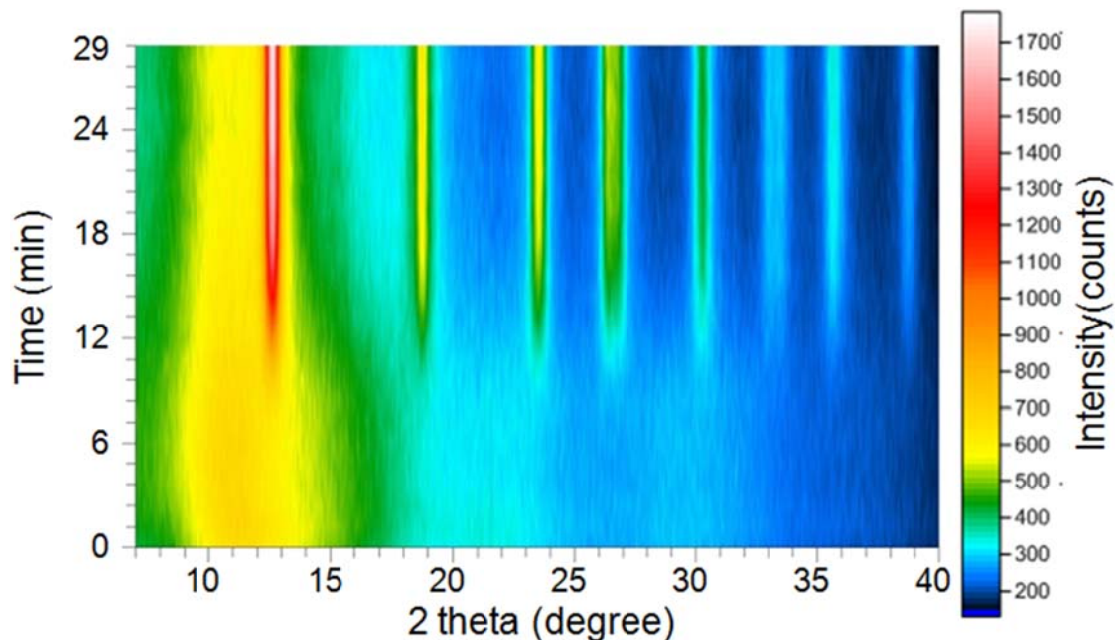


**Figure S8** Time evolution of *in situ* PXRD patterns (viewed down the intensity axis) for PD05 – crystallization of HDA-free porous beads of 830 nm diameter in 67 vol% ethanol at 140 °C.

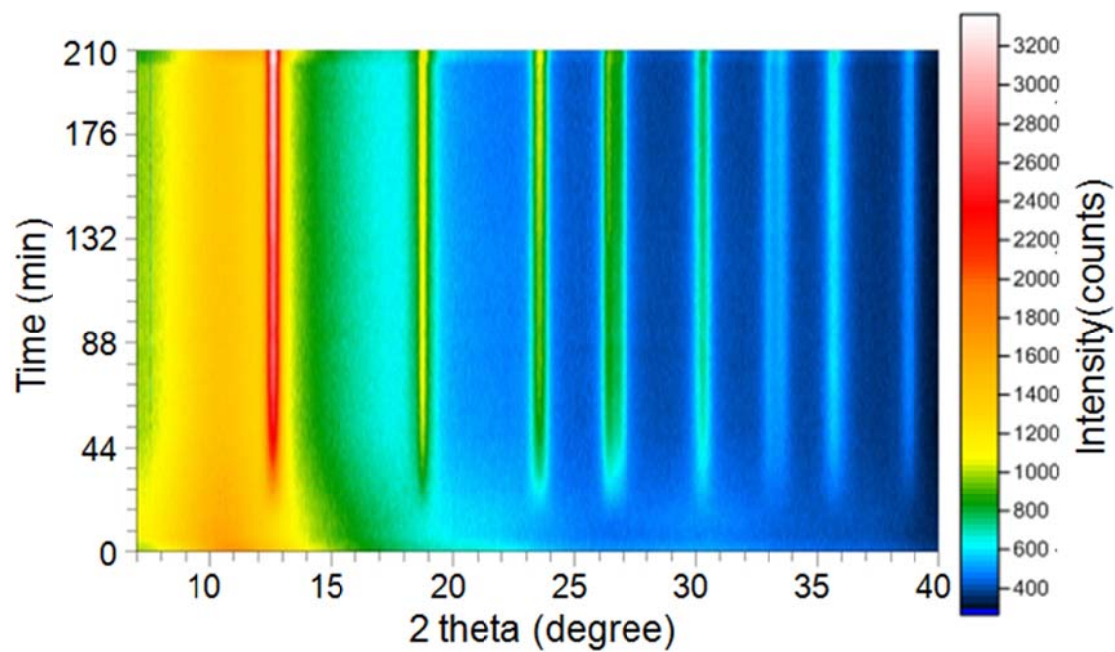


**Figure S9** Time evolution of *in situ* SR-PXRD patterns (viewed down the intensity axis) for PD06 – crystallization of bicontinuous TiO<sub>2</sub>/HDA hybrid beads of 1150 nm diameter in 80 vol% ethanol at 160 °C.

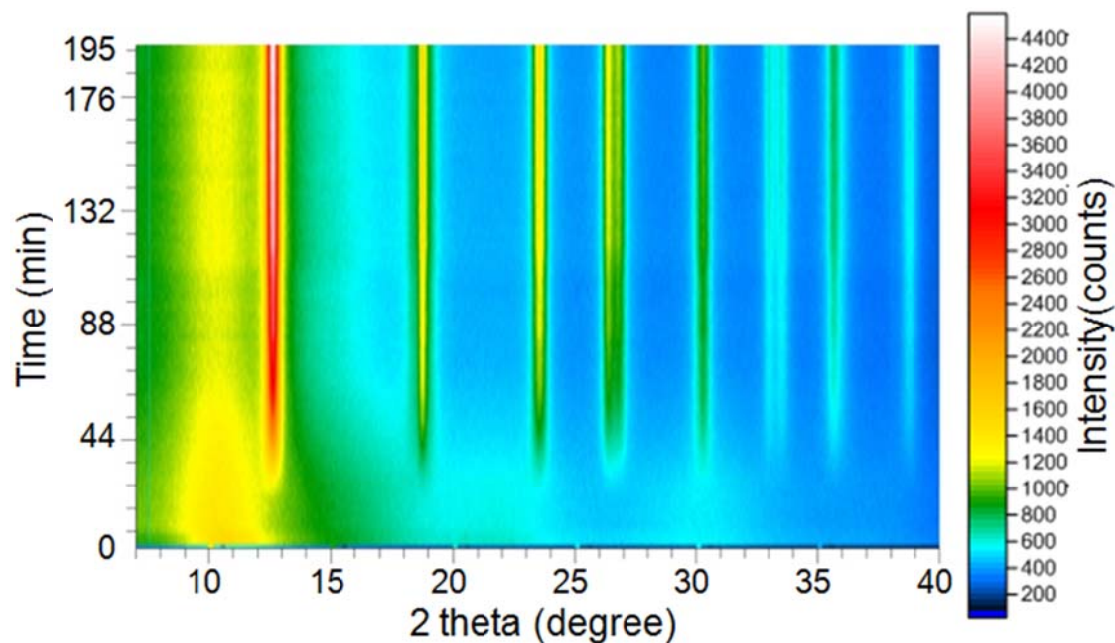


**Figure S10** Time evolution of *in situ* SR-PXRD patterns (viewed down the intensity axis) for PD07 – crystallization of bicontinuous TiO<sub>2</sub>/HDA hybrid beads of 1150 nm diameter in 91 vol% ethanol at 160 °C.

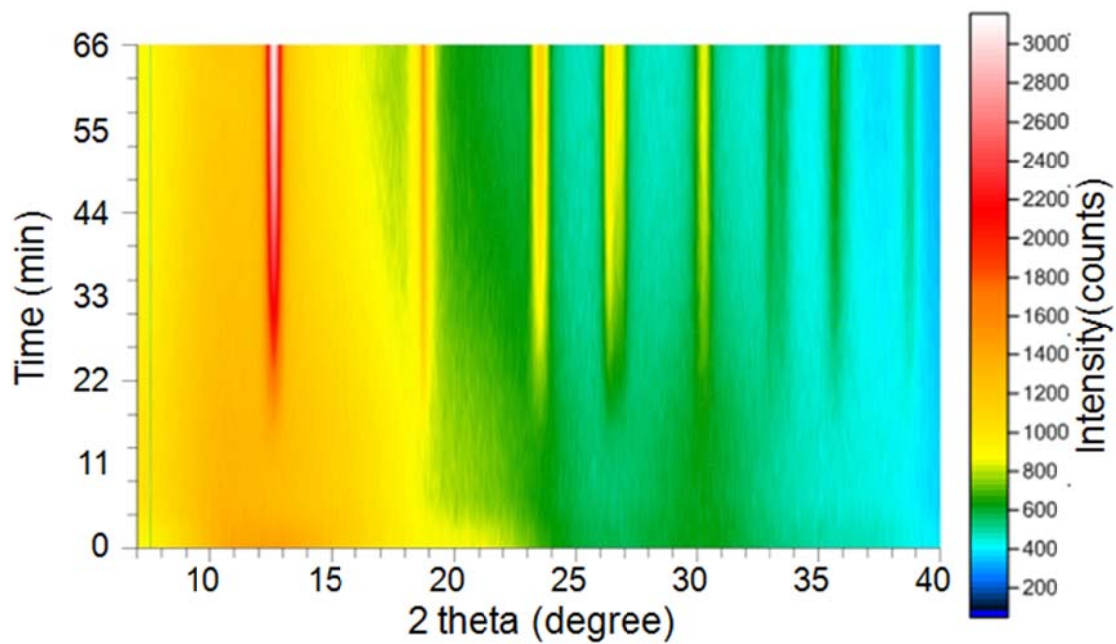


**Figure S11** Time evolution of *in situ* SR-PXRD patterns (viewed down the intensity axis) for PD08 – crystallization of bicontinuous TiO<sub>2</sub>/HDA hybrid beads of 1150 nm diameter in 67 vol% ethanol and 0.45 M ammonia at 160 °C.

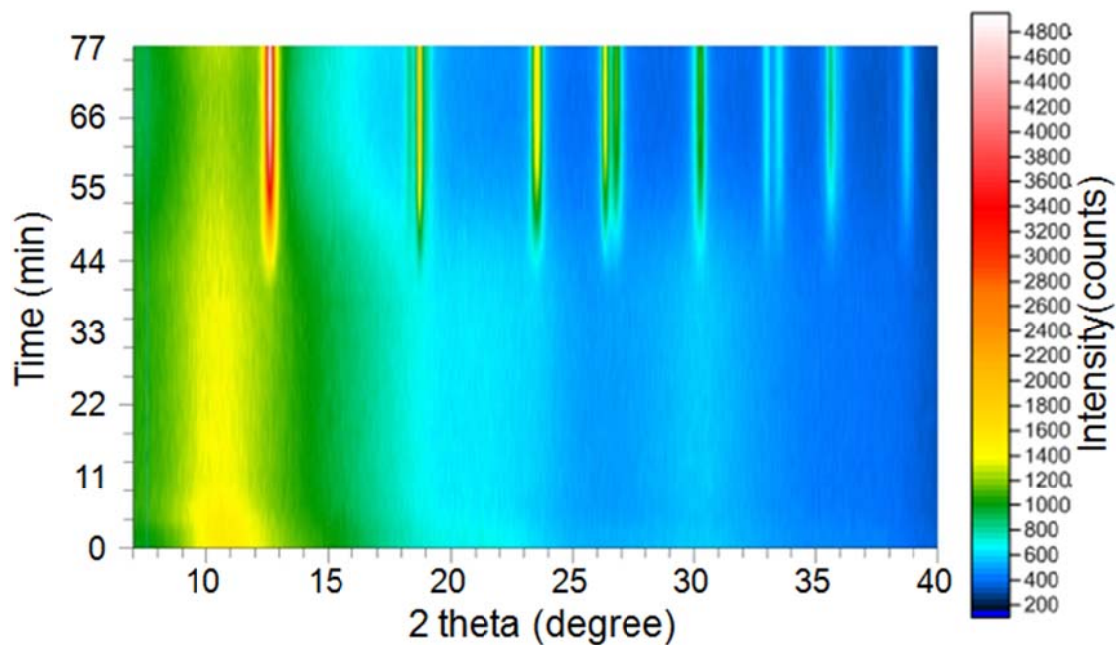


**Figure S12** Time evolution of *in situ* SR-PXRD patterns (viewed down the intensity axis) for PD09 – crystallization of bicontinuous TiO<sub>2</sub>/HDA hybrid beads of 1150 nm diameter in 67 vol% ethanol and 2.16 M ammonia at 160 °C.

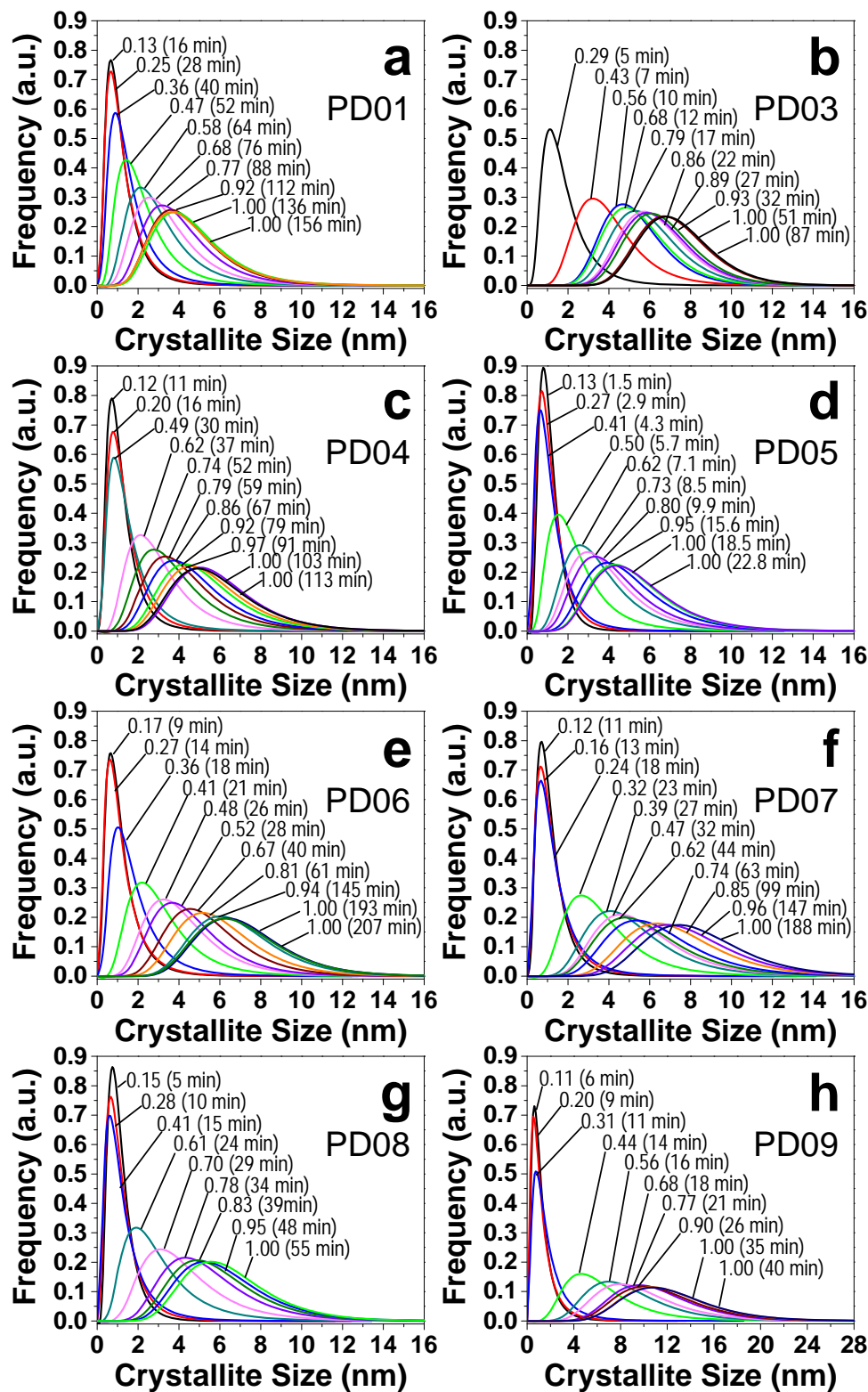


**Figure S13** Crystallite size distribution evolutions for (a) PD01, (b) PD03, (c) PD04, (d) PD05, (e) PD06, (f) PD07, (g) PD08, and (h) PD09; the number before the bracket is the extent of crystallization and in the bracket is the crystallization time (min) excluding induction time.

## References

- (1) Scardi, P.; Leoni, M. *Acta Crystallogr. Sect. A* **2002**, *58*, 190.
- (2) Leoni, M.; Confente, T.; Scardi, P. Z. *Kristall.* **2006**, *23*, 249.
- (3) Ilavsky, J.; Jemian, P. R. *J. Appl. Crystallogr.* **2009**, *42*, 347.
- (4) Beaucage, G. *J. Appl. Crystallogr.* **1995**, *28*, 717.